ORIGINAL ARTICLE

Direct growth of FeCo$_2$O$_4$ nanowire arrays on flexible stainless steel mesh for high-performance asymmetric supercapacitor

Nilesh R Chodankar[1], Deepak P Dubal[2], Yongchai Kwon[3] and Do-Heyoung Kim[1]

Currently, one-dimensional nanostructured binary metal oxides attract a great attention in supercapacitors (SCs) application due to their rapid charge transportation. In this respect, different nanostructures of FeCo$_2$O$_4$ are designed by simply tuning the reaction temperature in hydrothermal synthesis. These nanostructures are directly grown on flexible stainless steel mesh and further applied as binder-free electrodes for SCs. The systematic study is carried out to confirm the relation between surface characteristics and electrochemical properties of FeCo$_2$O$_4$ thin film. Among different nanostructures, FeCo$_2$O$_4$ nanowire arrays exhibit hierarchical mesoporous structure and demonstrate good surface properties including high surface area and appropriate pore volume. As a consequence, relatively high specific capacitance of 1963 F g^{-1} is obtained for the FeCo$_2$O$_4$ nanowire electrode. Further, asymmetric SC is fabricated using nanowired-FeCo$_2$O$_4$ and nanoparticulated-MnO$_2$ thin films as negative and positive electrodes with neutral Na$_2$SO$_4$ electrolyte. Impressively, the MnO$_2$//FeCo$_2$O$_4$ cell could be successfully cycled in a wide voltage window of 2.0 V, which can achieve a specific capacitance of 218 F g^{-1} and energy density of 43 Wh kg^{-1}. In addition, the SCs exhibit improved capacitance with cycling, which is attributed to opening of micro-pores occurred by frequent ion transport.

INTRODUCTION

Researchers and engineers have always focused on the development of efficient methods for energy production to improve the quality of human lives.[1,2] Fossil fuels are the major energy sources that are being used in the world today to fulfill the energy demand. However, the excessive consumption of fossil fuels leads to air pollution due to release of toxic gases such as CO$_2$, CO, NO$_2$ and SO$_2$. Consequently, obtaining energy from clean and safe renewable energy resources (like solar, wind and ocean energy) to reduce the air pollution is getting important. However, the energy obtained from renewable energy resources is uncertain and inconsistent as it depends upon environmental conditions. To overcome the difficulties, energy storage technology for storing the renewable energy should be developed.[3,4] Since the last decade, the industry and research institutes have made significant effort to develop inexpensive and proficient energy storage devices.[5]

Presently, Li-ion batteries (LIBs) and supercapacitors (SCs) are considered as the promising energy storage devices because of their excellent electrochemical capabilities.[6] Especially, SCs have garnered more attention than LIBs due to their outstanding electrochemical properties including high power capability, short charging time, ultrahigh operational life and safe operation.[7,8] However, low energy density (5–15 Wh kg^{-1}) of the current SC devices prevents them from being used as various advanced electronic gadgets. The energy density of SCs can be enhanced by increasing the specific capacitance (C) of electrode and/or the operation voltage (V), since $E = 0.5 \, CV^2$.[9–11] Nano-architectured electrode materials have the capability of providing a higher specific capacitance because of their unique surface properties like a higher surface to volume ratio, higher surface area and a short diffusion path, which is beneficial for creating abundant electrochemical reactions.[12] Hence, in the past, many electrode materials have been prepared by using different architectures (for example, nanowires, nanorods, nanoflakes, nanoflowers and so on) for SC applications. Besides that, asymmetric design of the SCs with different pseudocapacitive materials (different potential windows) in identical electrolytes efficiently has improved both operating potential window and resultant energy density. Therefore, it is imperative to select the proper nanostructured electrode material for asymmetric SC devices that are inexpensive, environmentally friendly and have superior electrochemical performance.

[1]School of Chemical Engineering, Chonnam National University, Gwangju, South Korea; [2]School of Chemical Engineering, The University of Adelaide, Adelaide, South Australia, Australia and [3]Graduate School of Energy and Environment, Seoul National University of Science and Technology, Seoul, South Korea
Correspondence: Professor Y Kwon, Graduate School of Energy and Environment, Seoul National University of Science and Technology, 232 Gongneung-ro, Nowon-gu, Seoul 01811, South Korea.
E-mail: kwony@seoultech.ac.kr
or Professor D-H Kim, School of Chemical Engineering, Chonnam National University, 77, Yongbong-ro, Buk-gu, Gwangju 61186, South Korea.
E-mail: kdhh@chonnam.ac.kr
Received 14 February 2017; revised 2 April 2017; accepted 18 June 2017

2

Transition metal oxides are the promising electrode materials for supercapacitors due to their low-cost, eco-friendliness, large abundance and redox activity and so on.[13–17] Recently, spinel-structured binary metal oxides are extensively tested for SC applications because they provide a very high specific capacitance (500–3000 F g^{-1}), electrical conductivity and better cycling stability compared to the single metal oxides (For comparison of binary and single metal oxides see Supporting information (SI) 1). In particular, MCo$_2$O$_4$ (M = Ni, Zn, Mn or Cu) has shown promising characteristics for SC applications.[18,19] The cationic substitutions of Co by any other metal cations (having a different oxidation state) effectively enhance electrical conductivity as well as electrochemical performance of the electrode.[20,21] In addition, for MCo$_2$O$_4$, it is assumed that both the metal cations take part in the redox reactions that will again contribute to additional specific capacitance.[22] Furthermore, there is a need to improve capacitive performance of the MCo$_2$O$_4$ electrode by substituting metal cations for Co. In that prospect, FeCo$_2$O$_4$ can provide excellent electrochemical characteristics than the corresponding single components because it undergoes redox reactions from both the cations. A few studies have reported the effects of FeCo$_2$O$_4$ electrodes on performance of SCs and battery applications although limited capacity was still roadblock to be overcome.[23–25]

In our study, we have designed a new high-performance asymmetric SCs using FeCo$_2$O$_4$ nanowires and MnO$_2$ nanoparticles in thin film form as negative and positive electrodes, respectively, in aqueous 1 M Na$_2$SO$_4$ electrolyte. Initially, the different nanostructures of FeCo$_2$O$_4$ were directly grown on the stainless steel mesh (SSM) by simply tuning the reaction temperatures of precursor in hydrothermal method. The SSM substrate not only provides conducting backbone, but it also maintains mechanical stability to the FeCo$_2$O$_4$ thin film. First, the electrochemical measurements of FeCo$_2$O$_4$ were performed in conventional three-electrode configuration with 1 M Na$_2$SO$_4$ electrolyte. In the next step, the MnO$_2$ thin film was prepared on a SSM substrate by a simple chemical bath deposition (CBD) method in order to use as positive electrode in asymmetric cell. Finally, the asymmetric cell with FeCo$_2$O$_4$ as negative and MnO$_2$ as positive electrode was assembled in 1 M Na$_2$SO$_4$ electrolyte. The electrochemical performances of the cell were tested with different techniques such as cyclic voltammetry, galvanostatic charge/discharge and electrochemical impedance.

EXPERIMENTAL PROCEDURES
Materials
All chemicals were analytical grade and used as received. Cobalt nitrate (Co(NO$_3$)$_2$·6H$_2$O), iron nitrate (Fe(NO$_3$)$_2$·6H$_2$O), hexamethylenetetramine (HMT) and ammonium fluoride (NH$_4$F) were purchased from Sigma-Aldrich. The SSM (200 mesh) substrate was purchased from Micro Mesh India Private Limited. All solutions were prepared in deionized water (DI).

Preparation of FeCo$_2$O$_4$ thin film on SSM
The preparation of FeCo$_2$O$_4$ thin films was performed in two steps; first, a hydrothermal process, and then thermal annealing in atmosphere were carried out. Before carrying out the chemical process, the SSM substrates were cleaned with 2 M HCl, DI water and acetone repeatedly for three times and then dried at 25 °C. Initially, 0.05 M of Fe(NO$_3$)$_2$·6H$_2$O and 0.1 M of Co(NO$_3$)$_2$·6H$_2$O were dissolved in 40 ml DI water with continuous stirring for 30 min. Subsequently, the 0.5 M HMT and 0.2 M NH$_4$F were added to the previously prepared solution and the entire solution was stirred for another 40 min to obtain a uniform distribution of each component. In the next step, the entire solution was transferred to a Teflon-lined stainless steel autoclave along with a well-cleaned piece of SSM substrate. The autoclave was maintained at different reaction temperatures of 80, 100, 120 and 140 °C for 12 h. After completing the

deposition, the autoclave was cooled to room temperature. Finally, the SSM substrate was removed from the autoclave, washed with DI water several times and dried at room temperature for 6 h. Further, the prepared brownish-colored thin films were annealed thermally in atmosphere at 350 °C for 3 h with the temperature increased at a rate of 3 °C min^{-1}. The active material deposited on the SSM is between 0.18 and 0.26 mg cm^{-2}. The SI 2 shows some images of the prepared samples before and after annealing with their mechanical flexibility. The FeCo$_2$O$_4$ thin films prepared at reaction temperatures of 80, 100, 120 and 140 °C are denoted as FCO80, FCO100, FCO120 and FCO140, respectively.

Supercapacitive measurements on FeCo$_2$O$_4$ thin films
The electrochemical features of the prepared FeCo$_2$O$_4$ thin films were evaluated using a three-electrode system that comprised of an as-prepared FeCo$_2$O$_4$ thin film, a platinum foil and a saturated calomel electrode (SCE) as the working, counter and reference electrodes, respectively, and 1 M Na$_2$SO$_4$ as the electrolyte. Cyclic voltammetry (CV) and galvanostatic charge-discharge (GCD) measurements were performed using an automatic battery cycler (WBCS3000) over the operating potential window of −1.0 to −0.3 V/SCE. The electrochemical impedance was assessed using an electrochemical workstation over the frequency range of 100 mHz to 100 kHz at a constant bias potential of 10 mV.

Fabrication of an aqueous MnO$_2$//FeCo$_2$O$_4$ asymmetric supercapacitor
In order to assemble the asymmetric SC devices, two electrodes are required with different operating potential windows that can work in the same electrolyte. MnO$_2$ is well known for its electrochemical features and it can operate over the positive potential range. Therefore, we prepared MnO$_2$ thin films on the SSM substrate by the CBD method. The details of the MnO$_2$ thin film synthesis are given in SI S8. The asymmetric SCs were assembled in a Swagelok cell, which contains the MnO$_2$ and FeCo$_2$O$_4$ thin films with the same area (1 cm^2) as the positive and negative electrode, respectively. A cellulose paper that acts as a separator was soaked in 1 M Na$_2$SO$_4$ electrolyte for 6 h and placed in between the two electrodes.

RESULTS AND DISCUSSION
In the thin film synthesis, reaction temperature plays a critical role in changing physical properties of the material such as surface morphology, porosity and crystallinity, and these physical properties are linked to electrochemical performances.[26] For the SC applications, these physical properties, such as smooth, uniform porous nanostructured thin films, are required in order to create an easy path for the electrochemical reaction.[27,28] Hence, nanostructured FeCo$_2$O$_4$ thin films on the SSM substrate at different reaction temperatures were prepared and their effects on electrochemical performance were studied systematically.

Initially, Figure 1 shows scanning electron microscopy (SEM) and the corresponding transmission electron microscopy (TEM) images of the FeCo$_2$O$_4$ thin films prepared at different reaction temperatures. From these micrographs, it was observed that surface morphology of the FeCo$_2$O$_4$ thin film was drastically changed from a nanoparticle to a horizontally aligned rhombus-shaped structure as the reaction temperature increased from 80 to 140 °C. Figure 1a and b represents surface morphology for the FCO80 thin film, which is composed of nanoparticles with a size of 400–600 nm. The corresponding TEM image of FCO80 thin film is also presented in the Figure 1c, which supported the SEM result because formation of nanoparticles was clearly appeared. As the autoclave temperature increased from the 80 to 100 °C, kinetics of the reaction were changed in terms of the nucleation, aggregation, coalescence and growth rate. The increasing temperature altered Brownian motion or short-range interaction of the solution particle. What is more, it changed inside pressure of the autoclave, modifying the surface morphology from nanoparticle to
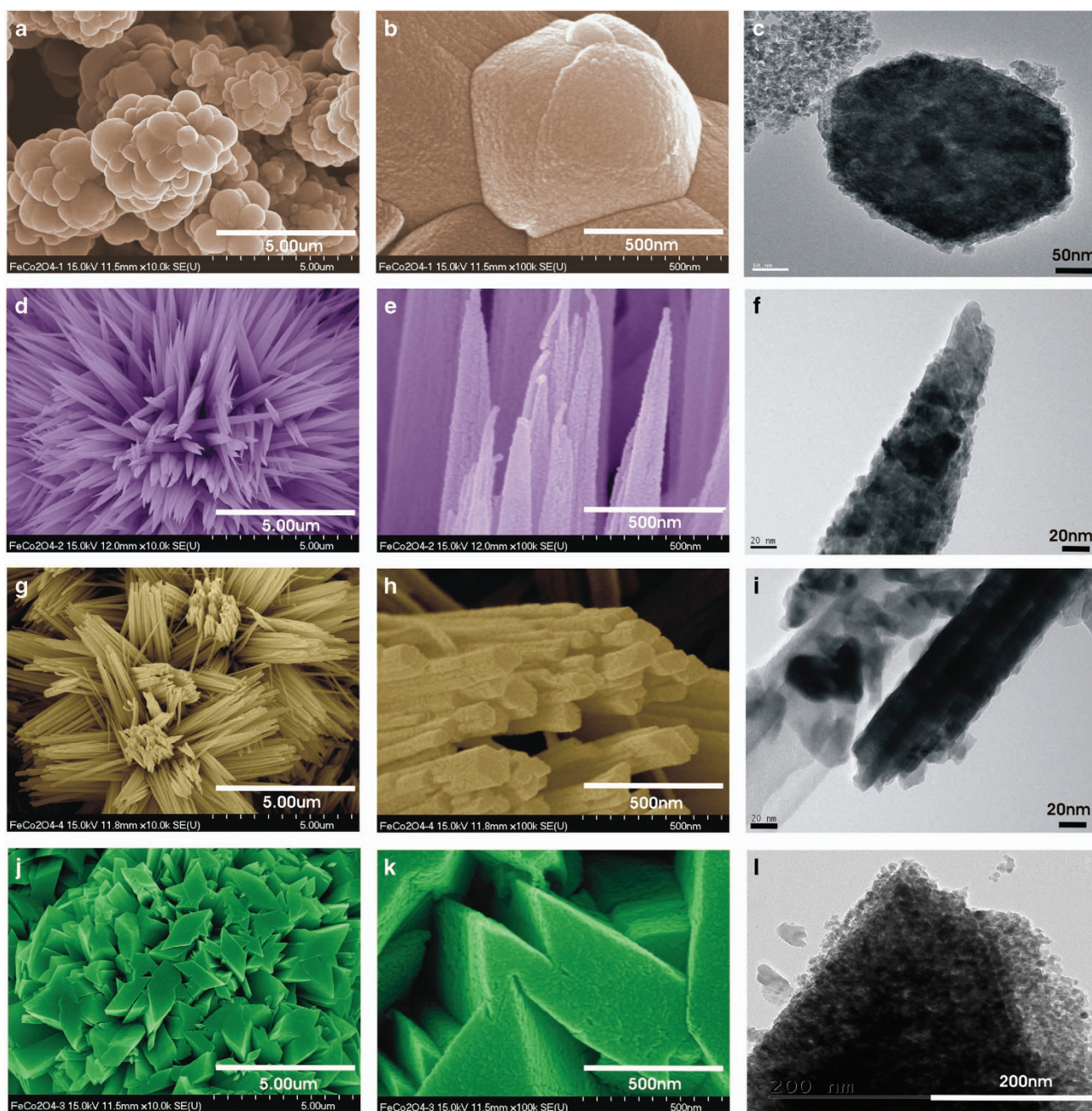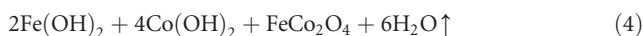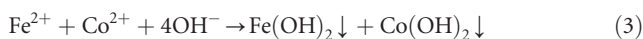
Figure 1 The SEM and the corresponding TEM images for FeCo$_2$O$_4$ thin films prepared at reaction temperature (**a–c**) 80 °C, (**d** and **e**) 100 °C, (**g–i**) 120 °C and (**j–l**) 140 °C.

nanoforest of nanowires (Figure 1d and e). These nanowires are uniform, vertically aligned and separated from each other, enabling abundant free space for the electrolyte ions to allow an easy insertion/desertion process. From the high-magnification SEM image (see Figure 1e), it is observed that walls of each nanowire are decorated with very fine nanoparticle-like structures, which allows more active sites for electrochemical reactions. The feature of these nanowires indicates that each nanowire has its own electrical contact with current collector, which effectively reduces equivalent series resistance by improving charge transfer kinetic. It was confirmed that FeCo$_2$O$_4$ nanowire had average diameters of about 76.6 nm, while average height of nanowires was in the range of 2.86 µm as shown in SI 2.

Such vertically aligned 1D nanowires of FeCo$_2$O$_4$ thin film are extremely valuable in energy storage devices, particularly for SC applications. Some additional SEM images for FCO100 thin film are presented in the SI 2 and 3. The SI 2 represents surface morphology of the FCO100 sample before and after thermal annealing and from these figures it was observed the there was no major change in its surface morphology. Besides that, an increase in reaction temperature (120 °C) leads to formation of a cluster of nanorods with diameters of ~80–180 nm (Figure 1g–i). These nanorods are slightly inclined horizontally, creating some obstacles for ion transport that play a role in improving charge transfer resistance of the electrode. Moreover, an increase in the reaction temperature results in compact and dense

4

irregular horizontal rhombus-shaped surfaces for the FCO140 thin film (Figure 1j and k). The increasing temperature limits vertical growth of the nanomaterial, which reduces its surface energy.[26] That is why, after 100 °C, the nanomaterial inclines in the horizontal direction to form aggregated nanorods and rhombus-shaped structure. The aggregated nanostructure does not allow access to the inner electro-active sites for the electrochemical reactions as it blocks path of the electrolyte ions.

The hydrothermal method works on principle of controlled precipitation under influences of temperature and pressure. At a constant temperature, thin film is formed on the substrate surface when the solution transforms from supersaturated state to saturated state in four different steps: nucleation, aggregation, coalescence and growth of the thin film. The degree of solution transport from the supersaturated state to the saturated state is dependent on temperature. The increasing reaction temperature may alter chemical reaction rate, which leads to formation of different nanostructures in Fe-Co hydroxide on the substrate surface.[29] The following chemical reactions (Equations 1–4) are involved in formation of the FeCo$_2$O$_4$ thin film on SSM substrate. In the first step, the hydrolysis of HMT occurs to form ammonia and OH$^-$ ions (Equations 1 and 2) in reaction medium and that are further reacted with metal cations to form Fe, Co hydroxide on SSM substrate (Equation 3). In the next step for converting the Fe, Co hydroxide into FeCo$_2$O$_4$, the prepared thin film was annealed thermally in atmosphere at 350 °C for 3 h (Equation 4).

$$C_6H_{12}N_4 + 6H_2O \rightarrow 4NH_3 + 6CH_2O \qquad (1)$$

$$NH_3 + H_2O \rightarrow NH_4^+ + OH^- \qquad (2)$$

$$Fe^{2+} + Co^{2+} + 4OH^- \rightarrow Fe(OH)_2\downarrow + Co(OH)_2\downarrow \qquad (3)$$

$$2Fe(OH)_2 + 4Co(OH)_2 + FeCo_2O_4 + 6H_2O\uparrow \qquad (4)$$

Porous nanostructured nature of the prepared FeCo$_2$O$_4$ thin films is also characterized by Brunauer-Emmett-Teller measurements. Figure 2a shows N$_2$ adsorption-desorption isotherms for the FeCo$_2$O$_4$ thin films prepared at different reaction temperatures, and Figure 2b displays Barrett-Joyner-Halenda pore size distribution. In order to obtain a higher energy storing capacity for the SCs, a larger specific surface area and appropriate pore volume are critical. The larger specific surface area of the electrode permits large electroactive sites for the electrolyte ions, while the appropriate pore volume promotes transportation of the electrolyte ions to reduce charge transfer resistance. The N$_2$ adsorption-desorption isotherms for all the samples belong to the type IV isotherms with H3 hysteresis loops that mostly take place over higher pressure (p/p$_0$) range of 0.6–1, which corresponds to mesoporous texture of the sample (Figure 2a).[11] Pore size distributions for nanoparticles, nanowires, nanorods and rhombus-like structure are mainly observed in the range from 2 to 20 nm, suggesting that they belong to mesoporous structure (Figure 2b). Calculated specific surface area for the FCO80, FCO100, FCO120 and FCO140 samples are 22, 47, 34 and 15 m^2 g^{-1}, respectively. The results indicate that the FCO100 sample exhibits relatively high specific surface area, pore volume (0.0076 cm^3 g^{-1}) and appropriate pore radius (~6 nm), which is beneficial for improving supercapacitive performance of the electrode. The results of the Brunauer-Emmett-Teller measurement support the SEM and TEM results. The vertically aligned nanowire (FCO100) shows a very high specific surface area and smaller pore radius compared to the other samples. Such nanostructured surface morphology is good for energy storage applications as it provides large active sites for the

electrochemical reaction. The nanorods (FCO120) and rhombus-like structure (FCO140) show a smaller specific surface area compared to the FCO100 sample because increasing temperature does not allow vertical growth of the nanomaterials that induce a reduction in charge storage capacity of the electrode material. Furthermore, the sample prepared at a lower temperature (FCO80) shows a smaller surface area than the FCO100 sample that is attributed to the larger nanoparticles (400–600 nm), and it is already well known that large nanoparticles have a lower specific surface area.[30]

The structural study of the prepared FeCo$_2$O$_4$ thin film was performed using X-ray diffraction, X-ray photoelectron spectroscopy and high-resolution transmission electron microscopy (HRTEM) measurements. All the X-ray diffraction peaks agree well with a cubic structure (JCPDS-98-009-8552) with the *Fd3m* space group (SI S4) and those are conveyed as (M)[M$'_2$]O$_4$, where M and M$'$ are the two metal cations that are arranged at the tetrahedral or octahedral site. In general, M is stayed at the tetrahedral A-site, while M$'$ is produced at the octahedral B-site. In spinel structure, Co exists as multiple oxidation states (+2 and +3). The high-spin Co^{2+} occupies tetrahedral A or octahedral B sites, while low-spin Co^{3+} only occupies octahedral sites. X-ray photoelectron spectroscopy measurements are carried out to confirm oxidation states of Fe, Co and O included in FCO100 thin film. The iron exists as Fe(II), whereas cobalt exists as the Co(II) and Co(III) oxidation state (SI S5). Figure 3a shows HRTEM image for the FCO100 thin film. The well-resolved lattice fringes can be assigned to cubic system of the FeCo$_2$O$_4$ thin film with the (113) plane. Additionally, energy-dispersive X-ray spectrometry analysis of the FCO100 sample (Figure 3b) shows that surface with the nanowires is formed only with Fe, Co and O having an atomic ratio of approximately 1:2:4, indicating that it forms pure phase. The elemental mapping images are presented in the Figure 3c–e for Fe, Co and O confirming the uniform distribution of each element all over the surface of thin film.

To determine operating potential range and best electrode for the SC applications, it is necessary to perform electrochemical evaluations. First, the CV measurements for all the FeCo$_2$O$_4$ thin films were performed in a 1 M Na$_2$SO$_4$ electrolyte over the operating potential range of −1.0 to −0.3 V/SCE at a constant scan rate of 100 mV s^{-1}, as seen in Figure 4a. In previous research, Perera et al.[31] also reported negative operating potentials with the uses of Co$_{3-x}$Mn$_x$O$_4$-based electrode and Li ion-based electrolyte, while their SC showed superior supercapacitive performance. From this figure, it was seen that all the CV curves for the FeCo$_2$O$_4$ thin film showed nearly rectangular shape even at a high scan rate of 100 mV s^{-1}, indicating that the thin film had superior supercapacitive behavior. Moreover, it was observed that the FCO100 thin film has a large CV area with higher anodic and catholic currents compared to the other samples, which suggests that it has greater ability to store the electrical charges in its nanostructure. Because of the nanowire structure of the FCO100 thin film and its higher electrical conductivity, a higher active surface area and optimum pore radius allows an easier path for electrochemical reactions. Similarly, charge-discharge measurements are performed at a constant current density of 2 mA cm^{-2} over the same operating potential range (Figure 4b), which showed similar results as those obtained in the CV measurements. As the FCO100 thin film takes more charging and discharging time than the other FeCo$_2$O$_4$ thin films, it proves that it has higher electroactive sites for the electrochemical reaction. Initial region of the discharge curve shows a certain potential (IR) drop although the degree of IR drop for the FCO100 thin film is very small compared to the other FeCo$_2$O$_4$ thin films. Comparatively, the rhombus-structured thin film shows a higher IR drop than the thin film composed of nanorods and the nanoparticles.

A schematic of the FCO100 thin film is presented in Figure 5. It contains a single thread of the SSM before and after the hydrothermal treatment. The each thread of the SSM permits electric current to pass through it and all the nanowires of FCO100 are connected to that of SSM thread, improving electrical conductivity of the electrode as well as reducing contact resistance of the electrode material with current collector. Additionally, each nanowire is separated from the other, allowing unrestricted movement of the electrolyte ions to perform the electrochemical reaction in inner side of the electrode as well. Hence, the FCO100 thin film demonstrates better electrochemical performance compared to the FCO80, FCO120 and FCO140 thin films. More importantly, in present study, we have used the Na$_2$SO$_4$ as an electrolyte for measuring the electrochemical performance of the FeCo$_2$O$_4$ thin films instead of KOH electrolyte. In literature, generally the electrochemical performance of the binary metal oxide is tested in the KOH electrolyte. But as we observed in the literature with KOH electrolyte, the binary metal oxide shows much distorted CV and charge-discharge shape, which is not an ideal supercapacitive characteristic. As in present case, we observed that the shape of the CV and charge-discharge curves have actual supercapacitor characteristics, indicating the better capacitive behavior with high energy storing efficiency for the FeCo$_2$O$_4$ thin film in the Na$_2$SO$_4$ electrolyte. In Na$_2$SO$_4$ electrolyte, electrochemical insertion/extraction process of Na$^+$ ion occurring in the FeCo$_2$O$_4$ electrode is controlled by the following reaction mechanism.[32]

$$FeCo_2O_4 + xNa^+ + xe^- \leftrightarrow Na_xFeCo_2O_4 \tag{5}$$

For the FeCo$_2$O$_4$, reversible charge storage occurred by a change in oxidation state of the transition metal (Fe and Co). The sodium ion is accommodated in oxide layer that is produced as a result of reduction reactions for Fe and Co without full conversion to Fe/Co metal. More importantly, the reversible charge storage occurred at the FeCo$_2$O$_4$-based electrode with no change in supercapacitive property, implying that the structure of FeCo$_2$O$_4$ is stable in the Na$_2$SO$_4$ electrolyte. Furthermore, to judge rate capability of the optimized FCO100 thin film, CV and charge-discharge measurements were performed at different scanning rates. From the CV curves (Figure 4c), it was observed that the FCO100 thin films maintained their CV profile irrespective of scan rate, representing better capacitive features of the thin film in a Na$_2$SO$_4$ electrolyte. As charging-discharging curves have an asymmetric nature, the curves (Figure 4d) confirm the
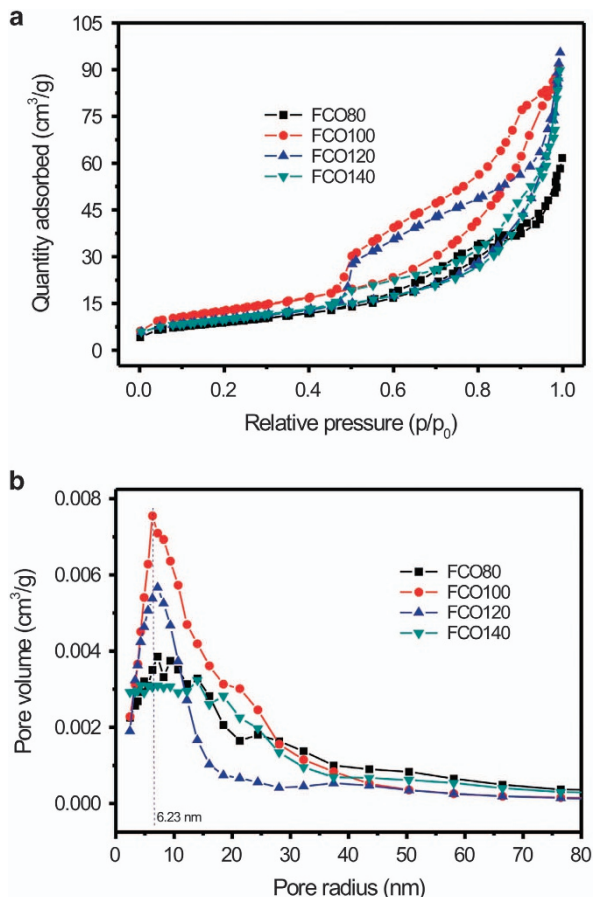

Figure 2 (a) The N$_2$ adsorption-desorption isotherms and (b) pore size distribution plot for FeCo$_2$O$_4$ thin films prepared at different reaction temperature.
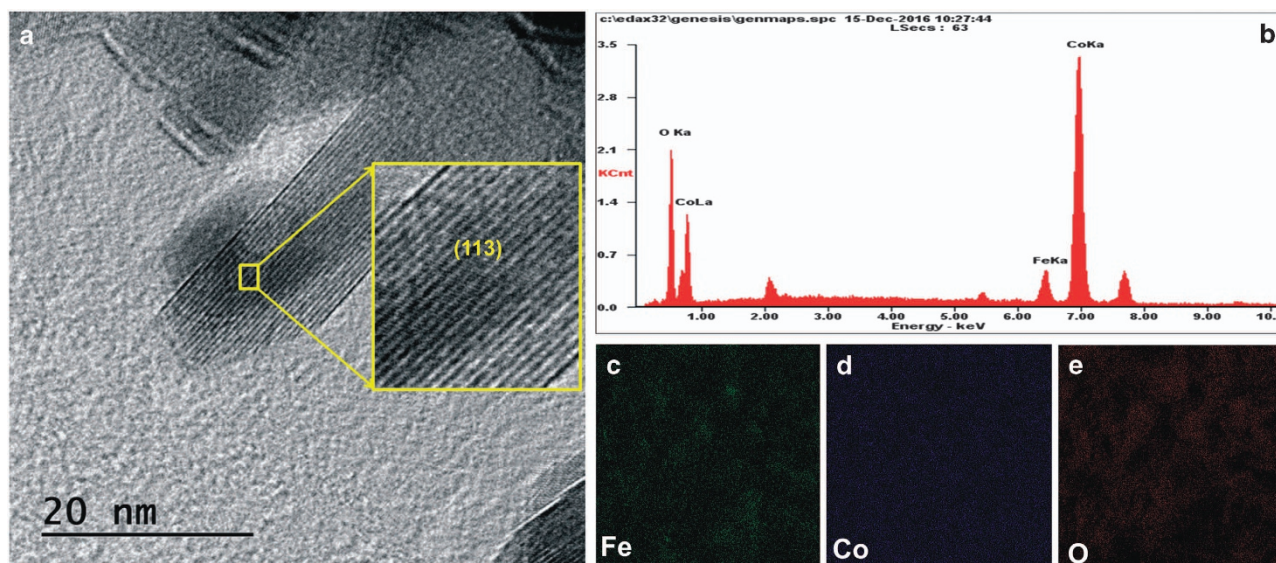

Figure 3 (a) HRTEM image and (b) the energy-dispersive X-ray spectrometry spectrum of FeCo$_2$O$_4$ prepared at 100 °C with corresponding mapping images for (c) Fe, (d) Co and (e) O.
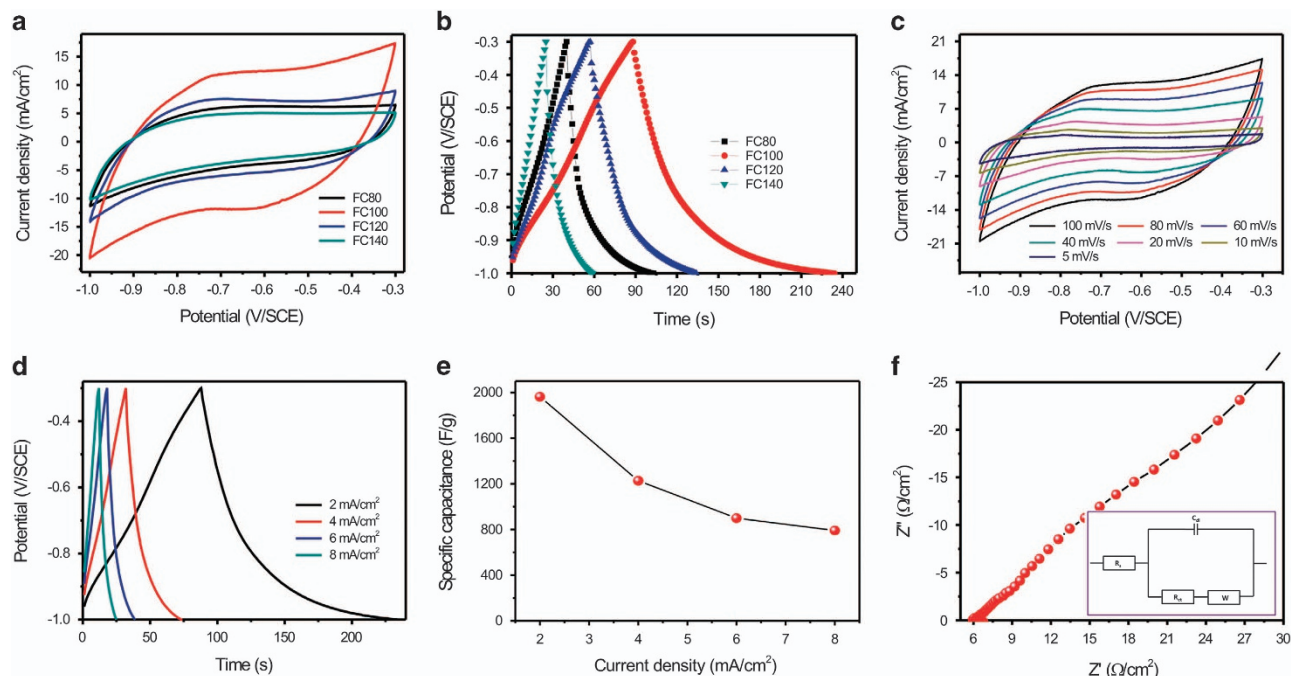
Figure 4 (**a**) CV curves for all FeCo$_2$O$_4$ thin films at constant scan rate of 100 mV s^{-1}, (**b**) the charge-discharge curves for all FeCo$_2$O$_4$ thin films at constant current density of 2 mA cm^{-2}, (**c**) CV curves and (**d**) charge-discharge curves for FeCo$_2$O$_4$ prepared at 100 °C at various scanning rate, (**e**) the plot of areal and specific capacitance with current density for FeCo$_2$O$_4$ prepared at 100 °C and (**f**) Nyquist plot for FeCo$_2$O$_4$ prepared at 100 °C, inset shows the equivalent circuit.
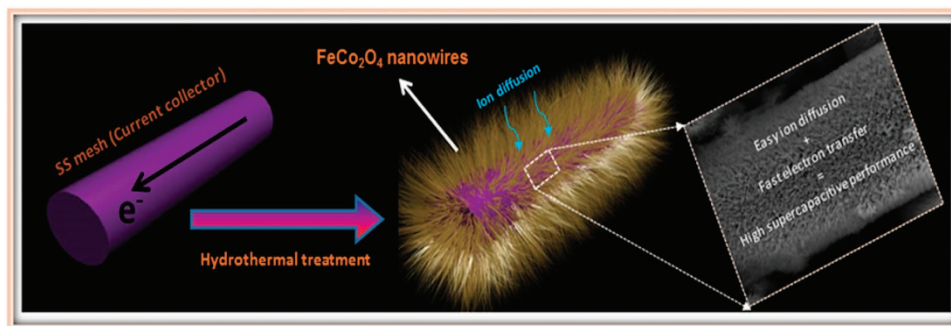

Figure 5 Schematic representations of stainless steel mesh thread before and after hydrothermal treatment to form the nanowires of FeCo$_2$O$_4$.

pseudocapacitive behavior. By using the discharge curve, the specific and areal capacitances were calculated at various current densities and are plotted in Figure 4e. The details of the specific capacitance calculation are given in the SI S13. At a lower current density of 2 mA cm^{-2}, the electrode shows a higher specific capacitance of 1963 F g^{-1} (393 mF cm^{-2}), whereas increasing the current density reduces value of the capacitance. The capacity reduction with the increasing current density can be attributed to the ineffective circulation of electrolyte ions at the higher current density, which agrees with previous reports. Obtained value of the capacitance is very high compared to previous results of the FeCo$_2$O$_4$ electrode.[23–25] This is attributed to the hierarchical nanowire structure, Na$_2$SO$_4$ electrolyte and SSM current collector. Also, the FCO100 thin film shows excellent electrochemical stability by maintaining 84.25% of its initial capacitance even after completing 5000 CV cycles (SI S7). Inset of the SI S7 represents the SEM image for FCO100 thin film before and after cycling. Since there is no change in the surface morphology of the FCO100 thin film even after 5000 CV cycles, it demonstrates that the prepared FCO100 thin film in Na$_2$SO$_4$ electrolyte maintains the better electrochemical stability. Further, to understand rate kinetics in terms of equivalent series resistance (R_s), charge-transfer resistance (R_{ct}) and Warburg impedance (Z_w), electrochemical impedance measurements were performed over the frequency range of 100 kHz–100 mHz at a constant bias potential of 10 mV. Figure 4f shows Nyquist plot for the FCO100 thin film that is divided into three parts of low, middle and high frequency ranges. The higher frequency region provides information about interfacial resistance of current collector to the electrode material and intrinsic resistance of the electrode material. The middle frequency range indicates how easily the electrolyte ions move inside the electrode material, while diffusion probability is obtained from the low frequency range. In general, the first intercept of the Nyquist plot to the real axis gives the R_s, while the magnitude of the semicircle gives the R_{ct}. In the present case, the FCO100 thin film shows very low R_s (5.8 Ω cm^{-2}) and R_{ct} (3.1 Ω cm^{-2}), suggesting good electrochemical response between the electrode material and the electrolyte ions. More importantly, the Nyquist plot makes an angle of 45° with the real axis, indicating resistive and capacitive behavior of the ions diffusing inside

pores of the FCO100 thin film. The inset of Figure 4f shows equivalent circuit obtained from the Nyquist plot.

To get more information about improved charge transfer kinetics for the FCO100 thin film in Na$_2$SO$_4$ electrolyte, we carried out additional analysis that is similar to the previous work.[31] In the analysis, total voltammetric charge (q) of the FCO100 electrode material was divided into two contributions: the surface capacitive (Q_s) and the diffusion-controlled charges (Q_d) as follow:

$$q = Q_s + Q_d \qquad (6)$$

In general, the capacitive charge contribution is mainly due to fast charge transfer kinetics at the interface of electrode/electrolyte and it corresponds to combination of faradic capacitance and double-layer capacitance. On the other hand, the diffusion-controlled charges are due to redox reaction of the bulk material and show slower kinetics than the capacitive contribution. By considering semi-infinite linear diffusion within reasonable scanning rate limit, the Q_s can be derived by (i) combination of total charges (q), reciprocal of square root of scan rate and (ii) extrapolation of ν to infinity with following equation:

$$q = Q_s + c\nu^{-1/2} \qquad (7)$$

where, c is the constant and ν is the scanning rate. Figure 6a represents plot of q against reciprocal of square root of scan rate. At a higher scanning rate, deviation in the linearity was observed due to polarization effect and this factor was ignored in the above equation.[33] Figure 6b shows plot of capacitive and diffusion-controlled contribution to total capacity at various scanning rate. Form the plot, it was clearly seen that the Q_s was prominent at a higher scan rate, while the Q_d was prominent at a lower scanning rate. The contribution of Q_s increases from 28.93 to 61.55% as scanning rate increases from 5 to 60 mV s^{-1}. On the same time, the reduction in the diffusion-controlled process is observed from 71.06 to 38.44% as scanning rate increases from 5 to 60 mV s^{-1}. This result strongly indicates that most of the FeCo$_2$O$_4$ intercalation sites are accessible to electrolyte ions at a lower scan rate.

Considering excellent electrochemical features of the FCO100 thin film, the asymmetric SCs are constructed (after balancing the charges of both electrodes) using FeCo$_2$O$_4$ (FCO100) and MnO$_2$ thin films as negative and positive electrodes, respectively, in 1 M Na$_2$SO$_4$ electrolyte. The details of the MnO$_2$ synthesis, X-ray photoelectron spectroscopy measurements, surface morphology, surface area calculation and its electrochemical features are discussed in the SI S8–11. The FeCo$_2$O$_4$ thin film is operated in negative potential (−1.0 to −0.3 V/

SCE) range, whereas the MnO$_2$ is operated in positive potential (0 to +1.0 V/SCE) range in the same electrolyte (see SI S12), it is possible to assemble these two electrodes in asymmetrically to enhance operating potential range as well as energy density of the SC devices. After assembling the MnO$_2$//FeCo$_2$O$_4$ asymmetric SCs, the first task is to optimize the operating potential range of the SCs to maintain reversibility of both electrode materials. Figure 7a displays the CV curves for the MnO$_2$//FeCo$_2$O$_4$ asymmetric SCs device at different operating potential ranges from 1.0 to 2.2 V. The optimized potential range for the MnO$_2$//FeCo$_2$O$_4$ asymmetric SCs device is 2.0 V. As the CV curves maintain their profiles up to 2.0 V, further increase in the potential disturbs cathodic shape of the CV curve. This means that up to 2.0 V, the electrode materials (FeCo$_2$O$_4$ and MnO$_2$) are capable of undergoing the reversible electrochemical reactions. More importantly, the obtained potential range is higher than that of previously reported asymmetric SCs. For example, Kong et al.[34] reported a potential of 1.6 V for the NiCo$_2$O$_4$@PPy//AC asymmetric SC devices (for more details see SI S15). Figure 7b shows the CV curves for MnO$_2$//FeCo$_2$O$_4$ asymmetric SC devices at various scan rates (5–100 mV s^{-1}). All the CV curves maintain their shape irrespective of scan rate, indicating the asymmetric SC devices show excellent capacitive behaviors. The maximum specific capacitance of 218 F g^{-1} (1.366 F cm^{-3}) was obtained at lower scan rate, whereas it was reduced to 94 F g^{-1} (0.54 F cm^{-3}) at a higher scan rate of 100 mV s^{-1} (Figure 7c).

To obtain more insight into supercapacitive features of the MnO$_2$//FeCo$_2$O$_4$ asymmetric SC devices, the charge-discharge profiles were measured at various current densities (1–9 mA cm^{-2}) and they are plotted in Figure 7d. The maximum specific and volumetric capacitance for the MnO$_2$//FeCo$_2$O$_4$ asymmetric SC devices reached 170 F g^{-1} and 1.066 F cm^{-3}, respectively, at a current density of 1 mA cm^{-2} (Figure 7e). The specific energy and power were calculated by considering the discharge curve and plotted as a Ragone plot (Figure 7f). The MnO$_2$//FeCo$_2$O$_4$ asymmetric SC devices showed the highest specific energy of 43 Wh kg^{-1} (26.66 mWh cm^{-3}) at a specific power of 800 Wh kg^{-1} (5000 mW cm^{-3}). Moreover, the obtained values of specific capacitance and specific energy for the MnO$_2$//FeCo$_2$O$_4$ asymmetric SCs were acceptable and these were much higher compared to previous results of the metal oxide-based asymmetric SCs such as NiCo$_2$O$_4$-rGO//AC (12 Wh·kg^{-1}, 1 M NaOH),[35] NiCo$_2$O$_4$//AC (12 Wh·kg^{-1}, 1 M NaOH),[36] NiCo$_2$O$_4$@MnO$_2$//AC (35 Wh·kg^{-1}, 1 M NaOH),[37] NiCo$_2$O$_4$//AC
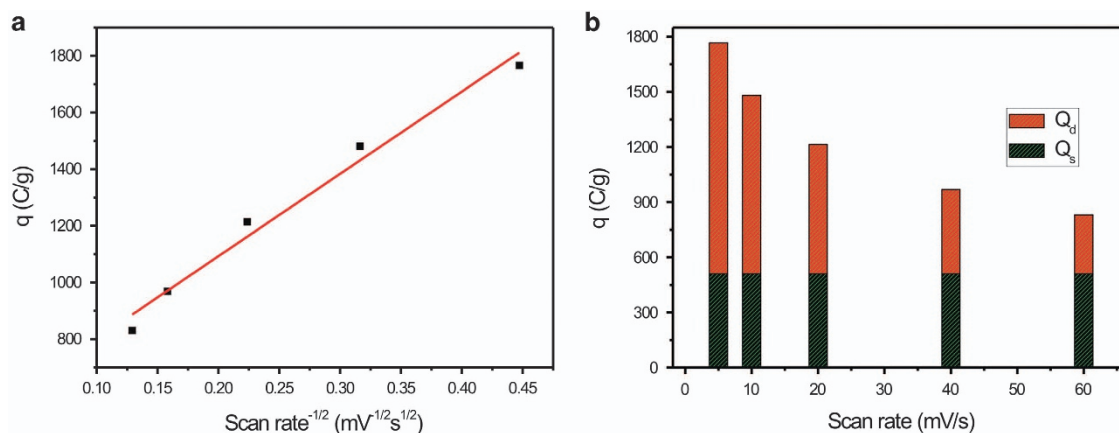

Figure 6 (a) The plot of total gravimetric charge (q) against the reciprocal of the square root of potential scan rate, (b) illustration of the contributions from the capacitive (Q_s) and diffusion-controlled (Q_d) charge to the total charge stored, at different scan rates.
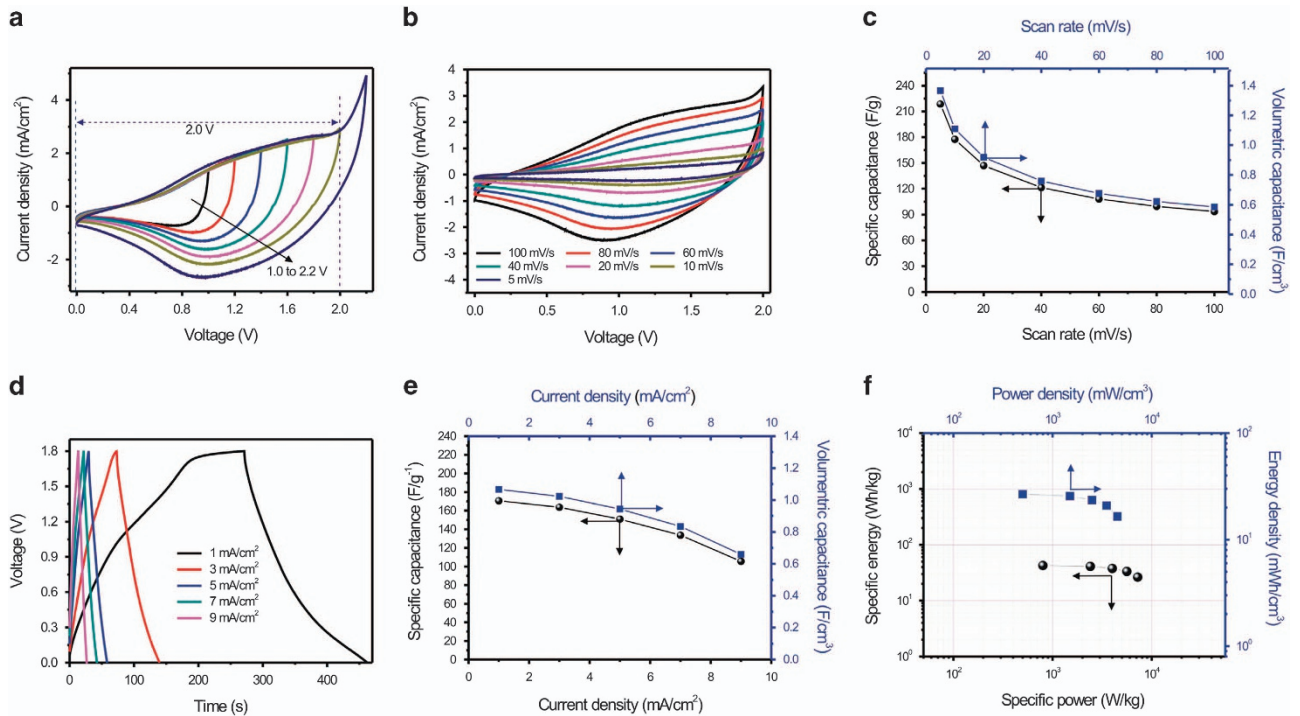
Figure 7 (**a**) CV curves for MnO$_2$//FeCo$_2$O$_4$ asymmetric SCs device at different potential range ranging from 1.0 to 2.2 V, (**b**) CV curves for MnO$_2$//FeCo$_2$O$_4$ asymmetric SCs device at different scan rate within operating potential range of 0-2.0 V, (**c**) the plot of specific and volumetric capacitance versus scan rate for MnO$_2$//FeCo$_2$O$_4$ asymmetric SCs device, (**d**) the charge-discharge curves for MnO$_2$//FeCo$_2$O$_4$ asymmetric SCs device at various current density, (**e**) the plot of specific and volumetric capacitance versus current density for MnO$_2$//FeCo$_2$O$_4$ asymmetric SCs device and (**f**) the Ragone plot for the plot of specific and volumetric capacitance versus scan rate for MnO$_2$//FeCo$_2$O$_4$ asymmetric SCs device.

(13.8 Wh·kg^{-1}, 1.5 M NaClO$_4$ in PC+DMC),[38] Co(OH)$_2$/GNS//AC/CFP (19.3 Wh·kg^{-1}, 1 M KOH),[39] NiO//Fe$_2$O$_3$ (12.4 Wh kg^{-1}, PVA/KOH),[40] Ni-Co LDH/3D RGO NF//AC (38.6 Wh kg^{-1}, 6 M KOH)[26] (for more details see SI S15). The higher specific energy for the MnO$_2$//FeCo$_2$O$_4$ asymmetric SC devices was resulted from higher operating potential (2.0 V) and higher capacitance of the device.

Cycling stability is another serious issue for the SC devices and long-term cycling stability is required for its commercialization.[41] Cycling test of MnO$_2$//FeCo$_2$O$_4$ asymmetric SCs device was performed over 5500 CV cycles at a constant scan rate of 50 mV s^{-1} at a potential window of 2.0 V (Figure 8a). The device conserves 86.05% of its initial capacitance even after 5500 CV cycles, indicating that cycling stability of the MnO$_2$//FeCo$_2$O$_4$ asymmetric SC devices was good (Figure 8b). From Figure 8b, it was observed that capacitance of the asymmetric SC device gradually increased during the initial 400 cycles, and in subsequent cycles, decrease in the capacitance was not significant. The increase in capacitance indicates that there is an initial activation of the electrode material that will open-up inner active sites for the electrochemical reactions.[42–45] More importantly, during the first 400 cycles the ~ 1.75-fold increment is observed in the capacitance and after that in the capacity is observed. Therefore, it is essential to calculate the capacity retention of the asymmetric supercapacitor by considering the 400th cycle as the reference cycle. By considering this factor, we observed the asymmetric devices retains about 52% of the initial capacitance even after the 5500 CV cycles, which suggest the better supercapacitive features of the developed asymmetric supercapacitor. The electrochemical impedance spectroscopy measurements were performed before and after cycling to obtain more information regarding the capacitance fading after 5500 CV cycles. Figure 8c shows Nyquist plot, from which it was observed

that the asymmetric device had lower ESR and R_{ct} values that were lower than 10 Ω cm^{-2}. In addition, the inset shows equivalent circuit fitted for standard data, which contain the R_s, R_{ct}, C_{dl}, Warburg impedance (W) and constant phase elements. The constant phase element is occurred in the Nyquist plot due to non-uniform pore distribution by inhomogeneous charge accumulation at electrode/electrolyte interface. Further, only a little increase in the resistance values was observed after 5500 cycles, suggesting the better capacitive features of the MnO$_2$//FeCo$_2$O$_4$ asymmetric SC devices. This small increase in the resistance may arise because of detachment of the electrode material from current collector.[46] Moreover, self-discharge is a rarely discussed parameter for SCs in the literature. Here we have also measured the self-discharge time for the MnO$_2$//FeCo$_2$O$_4$ asymmetric SC device by charging at a constant current of 1 mA cm^{-2} (Figure 8d). The self-discharge time of the asymmetric SC device was excellent because it maintained its potential (0.6 V) even after 18 h. These results indicate the effectiveness of the MnO$_2$//FeCo$_2$O$_4$ asymmetric SC devices for practical applications.

The excellent electrochemical performance of the MnO$_2$//FeCo$_2$O$_4$ asymmetric SC device was ascribed to interactive contribution of both electrode materials (FeCo$_2$O$_4$ and MnO$_2$) and electrolyte. Namely, superiority of the MnO$_2$//FeCo$_2$O$_4$ asymmetric SC device is because (1) binder-less and additive-free synthesis approach of the thin film (for FeCo$_2$O$_4$ and MnO$_2$ thin film) effectively removes dead surface area and resistance of the binder/additive, (2) the small diameter of the nanowires leads to a high surface area, which undoubtedly contributes to the high capacitance, (3) the well-defined array structure of nanowires leads to the separation of neighboring 1D nanostructures from each other and makes most of the surface of nanowires easily accessible by the electrolyte. This will give high capacitance and
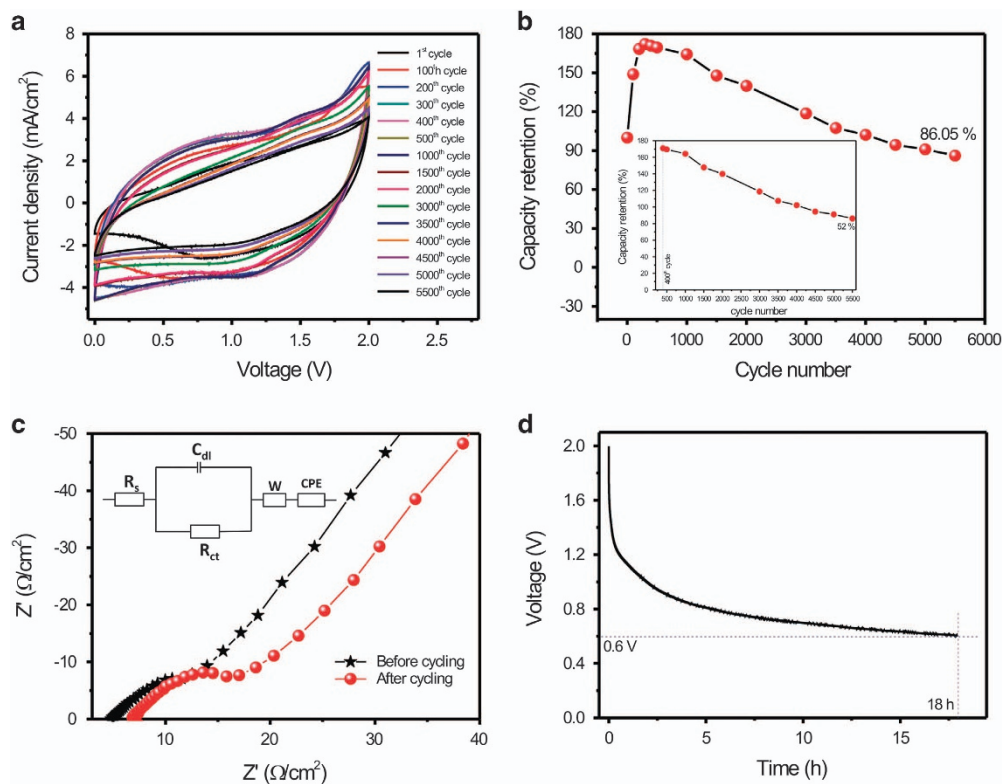
Figure 8 (**a**) CV curves for MnO₂//FeCo₂O₄ asymmetric SCs device for 5500 cycles, (**b**) the plot of capacity retention versus cycle number for MnO₂//FeCo₂O₄ asymmetric SCs device, inset shows the capacity retention from 400th cycle (**c**) before and after cycling Nyquist plot for MnO₂//FeCo₂O₄ asymmetric SCs device, inset shows the fitted equivalent circuit and (**d**) self-discharge measurement for MnO₂//FeCo₂O₄ asymmetric SCs device.

enhanced electrochemical kinetics relative to conventional film electrodes, (4) complementary potential windows of the FeCo₂O₄ and MnO₂ thin film in an identical electrolyte provide a higher potential limit for the asymmetric SCs and (5) MnO₂ comprising nanoparticles provides large active sites for electrochemical reactions. Additionally, the SSM provided a higher surface for material hosting and it promotes electron transport. These results gained by the present work are better than former reports in terms of (1) use of very simple and cost-effective synthesis approach for thin film preparation, (2) use of a cost-effective SSM substrate and electrode material and (3) simple assembly route for the asymmetric SC device. Therefore, our approach has the potential for fabricating highly energetic asymmetric SCs devices for future electronics technology. Further, investigations are being continued for improving the electrochemical performance of asymmetric SCs in terms of specific capacitance, energy density and cycling stability.

CONCLUSION

In summary, a simple, capable binder-less hydrothermal approach was used to prepare nanostructured FeCo₂O₄ thin films on SSM current collector. Simply by monitoring the reaction temperature of autoclave, FeCo₂O₄ thin films comprising different nanostructures (nanoparticles, nanowires, nanorods and rhombus-like structure) were formed. Unique hierarchical mesoporous nanoforest of FeCo₂O₄ nanowire arrays offer a very high surface area (47 m² g⁻¹) and appropriate pore volume to enhance the electrode/electrolyte interaction by minimizing circulation path for the electrolyte ions and electrons. These valuable features lead to excellent electrochemical performance in terms of a high operating potential (0.7 V/SCE), high specific capacitance (1963 F g⁻¹) and excellent electrochemical stability (84.25% after

5000 CV cycles) in an aqueous electrolyte, which are suitable for assembling the SCs device. The MnO₂//FeCo₂O₄ asymmetric SC devices work at a high operating potential of 2.0 V with a specific capacitance of 218.56 F g⁻¹ (1.366 F cm⁻³) at a scan rate of 5 mV s⁻¹. More significantly, the asymmetric SC device displays an excellent energy density of 43 Wh kg⁻¹ (26.6 mWh cm⁻³), with a power density of 7200 W kg⁻¹ (4500 mWh cm⁻³) along with long-term cycling stability (86.05% after 5500 CV cycles). These excellent electrochemical features of the MnO₂//FeCo₂O₄ asymmetric SC device indicate the potential of the FeCo₂O₄ nanowire arrays for a high-performance energy storage field especially for light-weight, small and eco-friendly electronic devices.

CONFLICT OF INTEREST

The authors declare no conflict of interest.

PUBLISHER'S NOTE

Springer Nature remains neutral with regard to jurisdictional claims in published maps and institutional affiliations.

1 Xiong, X., Zhao, B., Ding, D., Chen, D., Yang, C., Lei, Y. & Liu, M. One-step synthesis of architectural Ni₃S₂ nanosheet-on-nanorods array for use as high-performance electrodes for supercapacitors. *NPG Asia Mat.* **8**, 300–307 (2016).

2 Chodankar, N., Dubal, D., Lokhande, A., Patil, A., Kim, J. & Lokhande, C. An innovative concept of use of redox-active electrolyte in asymmetric capacitor based on MWCNTs/MnO$_2$ and Fe$_2$O$_3$ thin films. *Sci. Rep.* **6**, 1–14 (2016).

3 Hou, Y., Chen, L., Liu, P., Kang, J., Fujit, T. & Chen, M. Nanoporous metal based flexible asymmetric pseudocapacitors. *J. Mater. Chem. A* **2**, 10910–10916 (2014).

4 Gund, G., Dubal, D., Shinde, S. & Lokhande, C. Architectured morphologies of chemically prepared NiO/MWCNTs nanohybrid thin films for high performance supercapacitors. *ACS Appl. Mater. Interfaces* **6**, 3176–3188 (2014).

5 Aricò, A., Bruce, P., Scrosati, B., Tarascon, J. & Schalkwijk, W. Nanostructured materials for advanced energy conversion and storage devices. *Nat. Mater.* **4**, 366–377 (2005).

6 Zhu, Y., Wu, Z., Jing, M., Hou, H., Yang, Y., Zhang, Y., Yang, X., Song, W., Jia, X. & Ji, X. Porous NiCo$_2$O$_4$ spheres tuned through carbon quantum dots utilized as advanced materials for an asymmetric supercapacitor. *J. Mater. Chem. A* **3**, 866–877 (2015).

7 Meng, G., Yang, Q., Wu, X., Wan, P., Li, Y., Lei, X., Sun, X. & Liu, J. Hierarchical mesoporous NiO nanoarrays with ultrahigh capacitance for aqueous hybrid supercapacitor. *Nano Energy* **30**, 831–839 (2016).

8 Kim, S., Kim, S., Jung, K., Kim, J. & Jang, J. Ideal nanoporous gold based supercapacitors with theoretical capacitance and high energy/power density. *Nano Energy* **24**, 17–24 (2016).

9 Chodankar, N., Dubal, D., Gund, G. & Lokhande, C. Bendable all-solid-state asymmetric supercapacitors based on MnO$_2$ and Fe$_2$O$_3$ thin films. *Energy Technol.* **3**, 625–631 (2015).

10 Chang, J., Jin, M., Yao, F., Kim, T., Le, V., Yue, H., Gunes, F., Li, B., Ghosh, A., Xie, S. & Lee, Y. Asymmetric supercapacitors based on graphene/MnO$_2$ nanospheres and graphene/MoO$_3$ nanosheets with high energy density. *Adv. Funct. Mater.* **23**, 5074–5083 (2013).

11 Zhou, Y., Xu, H., Lachman, N., Ghaffari, M., Wu, S., Liu, Y., Ugure, A., Gleasone, K., Wardle, B. & Zhang, Q. Advanced asymmetric supercapacitor based on conducting polymer and aligned carbon nanotubes with controlled nanomorphology. *Nano Energy* **9**, 176–185 (2014).

12 Zheng, Y., Yang, Y., Chen, S. & Yuan, Q. Smart, stretchable and wearable supercapacitors: prospects and challenges. *CrystEngComm* **18**, 4218–4235 (2016).

13 Frackowiak, E. Carbon materials for supercapacitor application. *Phys. Chem. Chem. Phys.* **9**, 1774–1785 (2007).

14 Kwon, S., Lee, E., Kim, B., Kim, S., Lee, B., Kim, M. & Jung, J. Preparation of activated carbon aerogel and its application to electrode material for electric double layer capacitor in organic electrolyte: effect of activation temperature. *Korean J. Chem. Eng.* **32**, 248–254 (2015).

15 Frackowiak, E. & Beguin, F. Carbon materials for the electrochemical storage of energy in capacitors. *Carbon* **39**, 937–950 (2001).

16 Yeom, D., Choi, J., Byun, W. & Lee, J. Manganese oxides nanocrystals supported on mesoporous carbon microspheres for energy storage application. *Korean J. Chem. Eng.* **33**, 3029–3034 (2016).

17 Lokhande, C., Dubal, D. & Joo, O. Metal oxide thin film based supercapacitors. *Curr. Appl. Phys.* **11**, 255–270 (2011).

18 Shi, F., Li, L., Wang, X., Gu, C. & Tu, J. Metal oxide/hydroxide-based materials for supercapacitors. *RSC Adv.* **4**, 41910–41921 (2014).

19 Shinde, N., Jagadale, A., Kumbhar, V., Rana, T., Kim, J. & Lokhande, C. Wet chemical synthesis of WO$_3$ thin films for supercapacitor application. *Korean J. Chem. Eng.* **32**, 974–979 (2015).

20 An, C., Wangn, Y., Huang, Y., Xu, Y., Jiao, L. & Yuan, H. Porous NiCo$_2$O$_4$ nanostructures for high performance supercapacitors via a microemulsion technique. *Nano Energy* **9**, 125–134 (2014).

21 Chen, Y., Zhu, J., Qu, B., Lun, B. & Xu, Z. Graphene improving lithium-ion battery performance by construction of NiCo$_2$O$_4$/graphene hybrid nanosheet arrays. *Nano Energy* **3**, 88–94 (2014).

22 Wu, Z., Zhu, Y. & Ji, X. NiCo$_2$O$_4$-based materials for electrochemical supercapacitors. *J. Mater. Chem. A* **2**, 14759–14772 (2014).

23 Mohamed, S., Chen, C., Chen, C., Hu, S. & Liu, R. High-performance lithium-ion battery and symmetric supercapacitors based on FeCo2O4 nanoflakes electrodes. *ACS Appl. Mater. Interfaces* **6**, 22701–22708 (2014).

24 Zhu, B., Tang, S., Vongehr, S., Xie, H., Zhu, J. & Meng, X. FeCo$_2$O$_4$ submicron-tube arrays grown on Ni foam as high rate-capability and cycling-stability electrodes allowing superior energy and power densities with symmetric supercapacitors. *Chem. Commun.* **52**, 2624–2627 (2016).

25 Pendashteh, A., Palma, J., Anderson, M. & Marcill, R. Nanostructured porous wires of iron cobaltite: novel positive electrode for high-performance hybrid energy storage devices. *J. Mater. Chem. A* **3**, 16849–16859 (2015).

26 Gund, G., Dubal, D., Jambure, S., Shinde, S. & Lokhande, C. Temperature influence on morphological progress of Ni(OH)$_2$ thin films and its subsequent effect on electrochemical supercapacitive properties. *J. Mater. Chem. A* **1**, 4793–4803 (2013).

27 Chodankar, N., Dubal, D., Gund, G. & Lokhande, C. Flexible all-solid-state MnO$_2$ thin films based symmetric supercapacitors. *Electrochim. Acta* **165**, 338–347 (2015).

28 Wu, G., Tan, P., Wang, D., Li, Z., Peng, L., Hu, Y., Wang, C., Zhu, W., Chen, S. & Chen, W. High-performance supercapacitors based on electrochemical-induced vertical-aligned carbon nanotubes and polyaniline nanocomposite electrodes. *Sci. Rep.* **43676**, 1–7 (2017).

29 Pudukudya, M., Hetieqa, A. & Yaako, Z. Synthesis, characterization and photocatalytic activity of annealing dependent quasi spherical and capsule like ZnO nanostructures. *Appl. Surf. Sci.* **319**, 221–229 (2014).

30 Chodankar, N., Gund, G., Dubal, D. & Lokhande, C. Alcohol mediated growth of α-MnO$_2$ thin films from KMnO$_4$ precursor for high performance supercapacitors. *RSC Adv.* **4**, 61503–61513 (2014).

31 Perera, S., Ding, X., Bhargava, A., Hovden, R., Nelson, A., Kourkoutis, L. & Robinson, R. Enhanced supercapacitor performance for equal Co-Mn stoichiometry in colloidal Co$_3$-xMnxO$_4$ nanoparticles, in additive-free electrodes. *Chem. Mater.* **27**, 7861–7873 (2015).

32 Chen, Z., Augustyn, V., Jia, X., Xiao, Q., Dunn, B. & Lu, Y. High-performance sodium-ion pseudocapacitors based on hierarchically porous nanowire composites. *ACS Nano* **6**, 4319–4327 (2012).

33 Chen, Z., Augustyn, V., Jia, X., Xiao, Q., Dunn, B. & Lu, Y. High-performance sodium-ion pseudocapacitors based on hierarchically porous nanowire composites. *ACS Nano* **6**, 4319–4327 (2012).

34 Kong, D., Ren, W., Cheng, C., Wang, Y., Huang, Z. & Yang, H. Three-dimensional NiCo$_2$O$_4$@polypyrrole coaxial nanowire arrays on carbon textiles for high-performance flexible asymmetric solid state supercapacitor. *ACS Appl. Mater. Interfaces* **7**, 21334–21346 (2015).

35 Hu, C., Hsu, C., Chang, K. & Hsu, H. Microwave-assisted hydrothermal annealing of binary Ni-Co oxy-hydroxides for asymmetric supercapacitors. *J. Power Sources* **238**, 180–189 (2013).

36 Hsu, C. & Hu, C. Synthesis and characterization of mesoporous spinel NiCo$_2$O$_4$ using surfactant-assembled dispersion for asymmetric supercapacitors. *J. Power Sources* **242**, 662–671 (2013).

37 Xu, K., Li, W., Liu, Q., Li, B., Liu, X., An, L., Chen, Z., Zou, R. & Hu, J. Hierarchical mesoporous NiCo$_2$O$_4$@MnO$_2$ core-shell nanowire arrays on nickel foam for aqueous asymmetric supercapacitors. *J. Mater. Chem. A* **2**, 4795–4802 (2014).

38 Ding, R., Qi, L., Jia, M. & Wang, H. An investigation of spinel NiCo$_2$O$_4$ as anode for Na-ion capacitors. *Electrochim. Acta* **114**, 726–735 (2013).

39 Zhao, C., Ren, F., Xue, X., Zheng, W., Wang, X. & Chang, L. A high-performance asymmetric supercapacitor based on Co(OH)$_2$/graphene and activated carbon electrodes. *J. Eletroanal. Chem.* **782**, 98–102 (2016).

40 Zhang, S., Yin, B., Wang, Z. & Peter, F. Super long-life all solid-state asymmetric supercapacitor based on NiO nanosheets and α-Fe$_2$O$_3$ nanorods. *Chem. Eng. J.* **306**, 193–203 (2016).

41 Bai, X., Liu, Q., Zhang, H., Liu, J., Li, Z., Jing, X., Yuan, Y., Liu, L. & Wang, J. Nickel-cobalt layered double hydroxide nanowires on three dimensional graphene nickel foam for high performance asymmetric supercapacitors. *Electrochim. Acta* **215**, 492–499 (2016).

42 Wei, B., Chen, C., Chien, H., Lu, S. & Hu, C. A cost-effective supercapacitor material of ultrahigh specific capacitances: spinel nickel cobaltite aerogels from an epoxide-driven sol-gel process. *Adv. Mater.* **22**, 347–351 (2010).

43 Wu, Y. & Hu, C. Effects of electrochemical activation and multiwall carbon nanotubes on the capacitive characteristics of thick MnO$_2$ deposits. *J. Elecrochem. Soc.* **151**, A2060–A2066 (2004).

44 Huang, Y., Shi, T., Jiang, S., Cheng, S., Tao, X., Zhong, Y., Liao, G. & Tang, Z. Enhanced cycling stability of NiCo$_2$S$_4$@NiO core-shell nanowire arrays for all-solid-state asymmetric supercapacitors. *Sci. Rep.* **38620**, 1–10 (2016).

45 Hu, C., Chang, K. & Hsu, T. The synergistic influences of OH$^-$ concentration and electrolyte conductivity on the redox behavior of Ni(OH)$_2$/ NiOOH. *J. Electrochem. Soc.* **255**, F196–F200 (2008).

46 Rakhi, R., Chen, W., Cha, D. & Alshareef, H. Substrate dependent self-organization of mesoporous cobalt oxide nanowires with remarkable pseudocapacitance. *Nano Lett.* **12**, 2559–2567 (2012).